International Journal of Fracture **101:** 161–180, 2000.
© 2000 *Kluwer Academic Publishers. Printed in the Netherlands.*

Finite element analysis of micromechanical failure modes in a heterogeneous ceramic material system

J. ZHAI and M. ZHOU*
The George W. Woodruff School of Mechanical Engineering, Georgia Institute of Technology, Atlanta, GA 30332-0405

Received 17 July 1998; accepted in revised form 28 April 1999

Abstract. A micromechanical model that provides explicit accounts for arbitrary microstructures and arbitrary fracture patterns is developed and used. The approach uses both a constitutive law for the bulk solid constituents and a constitutive law for fracture surfaces. The model is based on a cohesive surface formulation of Xu and Needleman and represents a phenomenological characterization for atomic forces on potential crack/microcrack surfaces. This framework of analysis does not require the use of continuum fracture criteria which assume, for example, the existence of K-fields. Numerical analyses carried out concern failure in the forms of crack propagation and microcrack formation. Actual microstructures of brittle alumina/titanium diboride (Al_2O_3/TiB_2) composites are used. The results demonstrate the effects of microstructure and material inhomogeneities on the selection of failure modes in this material system. For example, the strength of interfaces between the phases is found to significantly influence the failure characteristics. When weak interfacial strength exists, interfacial debonding and microcrack initiation and growth are the principal mode of failure. When strong interfacial strength is derived from material processing, advancement of a dominant crack and crack branching are observed.

Key words: Micromechanical modeling, cohesive force, fracture, heterogeneous materials, elasticity, fracture modes, failure modes, numerical simulation, crack propagation, ceramic composites.

1. Introduction

Microscopically inhomogeneous materials derive significantly higher strength and toughness from microscopic reinforcements such as fibers and particles. Composite materials with failure resistance superior to those of their individual constituents have been developed. The enhancement is due to the higher toughness and strength of the additional phases and deformation mechanisms that do not come into play for monolithic materials. In addition to different length scales associated with material inhomogeneities, different time scales are also introduced by composite microstructures under transient loading due to different stress wave speeds or the inertia effect. These spatial and temporal effects provide opportunities for material property enhancement. Material heterogeneities also give rise to multiple failure mechanisms. For example, fracture can occur in different phases and along phase boundaries in heterogeneous materials.

Ceramic composites with microstructural reinforcements over a range of size scales are emerging materials with increasing applications in heat engines, gas turbine blade coatings, cutting tools, drill bits, wear parts, sensors, magnetic recording media, structural components, electronic components, and biomedical devices (e.g. prosthetic articulate joints, orthopedic load-bearing hip implants, spinal surgery implants, dental crowns and bridges). These appli-

* To whom all correspondence should be addressed, *min.zhou@me.gatech.edu*, 404-894-3294.

cations take advantage of outstanding mechanical and thermomechanical properties at high temperatures (Lange, 1979; Zeng et al., 1992; Matsui et al., 1994), good wear resistance, high elastic moduli and excellent chemical stability (Jones, 1996) of the materials. For instance, ceramic nanocomposites make high performance cutting tools for high-speed machining (Komanduri, 1989). Ceramic composites are also excellent biomaterials since they are biocompatible (fully oxidized and chemically stable) and do not cause adverse effects within a physiological environment. Conversely, their reliability and performance are unaffected by the biological environment in a body. An important issue for ceramic materials in these applications, industrial or biomedical, is their failure resistance, including strength and fracture toughness (Komanduri, 1989; Messer, 1995). The fracture toughness of these materials is at least an order of magnitude lower than those of metals and polymers. Low failure resistance is the most important impediment to their applications, e.g. Willmann (1996a, b). Progress has been made in developing advanced ceramic materials using the fact that the materials derive significantly higher toughness from microscopic or nanosized reinforcements, (Niihara et al., 1990, 1991; Lehman, 1989; Zhao et al., 1993). For example, Niihara et al. (1993) reported that a 5 percent population of SiC nanoparticles increases the tensile strength of Si_3N_4 from 350 MPa to 1 GPa and improves its fracture toughness from 3.25 MPa$\sqrt{\text{m}}$ to 4.7 MPa$\sqrt{\text{m}}$. Recently, alumina/titanium diboride (Al_2O_3/TiB_2) composites with a wide range of microstructural morphologies demonstrate a range of failure resistance and a strong dependence of fracture toughness on microstructure in experiments, (Logan, 1996). These materials are composed of titanium diboride (TiB_2) reinforcements embedded in a matrix of alumina (Al_2O_3). The principal mode of failure observed in experiments is transgranular fracture of Al_2O_3 when strong interfacial strength between the phases is obtained through processing. In contrast, the principal mode of failure is interfacial fracture through microcrack formation when a weak interfacial bonding between the constituents is found. Clearly, interfacial strength significantly influences the overall behavior of the composites. Although microstructure-induced, size-dependent toughening mechanisms at the micro and nano levels are demonstrated approaches for property enhancement, the physics for such effects has not been well quantified. In order to develop more advanced materials, it is necessary to characterize the influences of phase morphology, phase length scale, and interfacial behavior on failure behavior and fracture toughness of these materials.

The dynamic failure of brittle materials has been extensively analyzed by, e.g. Shockey et al. (1974), Grady and Kipp (1979), Lankford (1989), Shockey et al. (1985), Brockenbrough et al. (1988), Longy and Cagnoux (1989), Kishi et al. (1990), Curtin (1991), Shockey et al. (1990), Suresh et al. (1990), Yang et al. (1990), Evans (1991), Kishi (1991), Kobayashi (1991), Espinosa et al. (1992), Ahrens and Rubin (1983), Vekinis et al. (1993), Lankford (1994), Woodward et al. (1994), and Zhou and Curtin (1995). Most available models for the failure are, for the most part, continuum damage theories in which the net effect of fracture is idealized as a degradation of the elasticity modulus, see e.g. Seaman et al. (1985), Curran et al. (1987, 1993), Rajendran (1994), Johnson and Holmquist (1992), Walter (1992), Espinosa et al. (1992, 1995), Ravichandran et al. (1995), and Gao et al. (1997). While capturing the macroscopic or effective response, these models do not explicitly consider the discrete nature of fracture through crack growth and coalescence. Thus, the models lack the ability to account for the interaction between cracks and resolve specific failure modes and failure patterns. In addition, the effects of microstructural inhomogeneities of different size scales such as inclusions, fibers and grains on crack path and fracture toughness cannot be explicitly analyzed.

The complex morphologies of material microstructures preclude the application of analytical methods. Explicit micromechanical modeling and simulation represent a unique and attractive means for analyzing micro and meso failure mechanisms and for elucidating scaling laws. Through the consideration of representative samples of actual microstructures, the effects of various fracture mechanisms can be delineated. The required features of this framework should include

(1) explicit account of real, arbitrary material microstructures,
(2) explicit resolution of fracture in a non-constrained (arbitrary crack paths or microcrack patterns) manner, and
(3) freedom from limitations of fracture criteria applicable only over certain length scales (e.g. continuum criteria which assume the existence of K-fields).

Combined use of the cohesive surface approach of Xu and Needleman (1994, 1997) and bulk constitutive laws is a good candidate for providing such a framework. A similar technique has also been used by Camacho and Ortiz (1996) and Ortiz (1996) in the analysis of dynamic failure of materials.

A cohesive finite element method (CFEM) for explicit micromechanical fracture analysis is developed and used here. This approach involves the combined use of a cohesive surface characterization for crack surfaces and bulk constitutive laws for solid constituents. In addition to traditional finite elements, all boundaries between the finite elements are cohesive surfaces serving as potential crack paths. Like in Xu and Needleman (1994), the crack surfaces are regarded as cohesive surfaces exhibiting traction forces which are functions of interfacial separations. The concept of cohesive crack faces can be traced back to the pioneering work of Dugdale (1960) and Barrenblatt (1962). The additional interfacial discretization in the CFEM allows the cohesive surfaces to permeate the whole microstructure as an *intrinsic* part of the material characterization. Consequently, fracture is an *inherent* attribute of the discrete model. Explicit account is taken of arbitrary crack and microcrack patterns as well as of arbitrary microstructures. Intergranular and transgranular fractures evolve as natural outcomes of the cohesive responses within each constituent, the cohesion between the phases, and the bulk constitutive behavior of the phases. The cohesive relations represent phenomenological characterizations of atomistic attraction and repulsion forces which vary with inter-atomic displacements. It is surmised that characterizations of the inter-atomic interactions are possible on the nano, micro, meso and continuum levels. When combined with bulk constitutive laws appropriate at the corresponding length scales, these cohesive models can provide a unified framework for explicit account and simulation of fracture processes over multiple length scales. This novel approach does not require any *a priori* crack initiation or propagation criteria required by traditional fracture mechanics approaches, such as the attainment of critical values of stress intensity factors or maintenance of constant energy release rate. The difference is significant because the concept or validity of singular crack tip fields ceases to exist when one approaches the grain, subgrain, or atomic scales. Since the CFEM model has the inherent properties of deformation *and* fracture upon loading, it possesses a predictive power similar to that of discrete molecular dynamics models concerning fracture initiation, fracture path, crack speed and microcrack patterning.

Analyses in this paper focus on the TiB_2/Al_2O_3 material system developed by Logan (1996) because of its application potential and because of the fact that processing has been demonstrated to be an effective means to alter the mechanical properties of the materials through microstructural modification. This selection is also motivated by the opportunity for

a joint program combining micromechanical modeling, mechanical testing and materials synthesis aimed at improving the fracture resistance of a class of ceramic composites. While a specific material system is considered here, the approach for explicit fracture modeling can be directly applied to other material systems. Understanding of microstructure-induced toughening mechanisms is also directly relevant for other composite materials.

2. Problem formulation

To account for finite strain involved in crack tip regions, a Lagrangian finite deformation formulation is used. The independent variables are the position of a material point in the reference configuration $\mathbf{x}$, and time t. Relative to a fixed Cartesian frame $\{\xi^i\}$, a material point initially at $\mathbf{x}$ occupies position $\overline{\mathbf{x}}$ in the current configuration. The displacement vector and the deformation gradient are defined as $\mathbf{u} = \overline{\mathbf{x}} - \mathbf{x}$ and $\mathbf{F} = \partial\overline{\mathbf{x}}/\partial\mathbf{x}$, respectively. The principle of virtual work includes a contribution from the cohesive surfaces and is written as

$$\int_V \mathbf{s} : \delta\mathbf{F}\,\mathrm{d}V - \int_{S_{\text{int}}} \mathbf{T}\cdot\delta\boldsymbol{\Delta}\,\mathrm{d}S = \int_{S_{\text{ext}}} \mathbf{T}\cdot\delta\mathbf{u}\,\mathrm{d}S - \int_V \rho\frac{\partial^2\mathbf{u}}{\partial t^2}\cdot\delta\mathbf{u}\,\mathrm{d}V, \tag{1}$$

where $\mathbf{s} : \delta\mathbf{F} = s^{ij}\delta F_{ji}$, $\mathbf{s}$ is the nonsymmetric first Piola–Kirchhoff stress; $\boldsymbol{\Delta}$ is the displacement jump across a pair of cohesive surfaces; V, S_{ext} and S_{int} are the volume, external surface area and internal cohesive surface area, respectively, of the body in the reference configuration. The density of the material in the reference configuration is ρ. Also, $\delta\mathbf{F}$, $\delta\boldsymbol{\Delta}$, and $\delta\mathbf{u}$ denote admissible variations in $\mathbf{F}$, $\boldsymbol{\Delta}$ and $\mathbf{u}$ respectively. The traction vector $\mathbf{T}$ and the surface normal in the reference configuration $\mathbf{n}$ are related through $\mathbf{T} = \mathbf{n}\cdot\mathbf{s}$. The volumetric constitutive law is hyperelastic so that

$$\mathbf{S} = \frac{\partial W}{\partial\mathbf{E}}, \tag{2}$$

where $\mathbf{S} = \mathbf{s}\cdot\mathbf{F}^{-T}$ is the second Piola–Kirchhoff stress. The strain energy density W is taken to be

$$W = \tfrac{1}{2}\mathbf{E} : \mathbf{L} : \mathbf{E} \tag{3}$$

with

$$\mathbf{L} = \frac{E}{1+\nu}\left(\mathbf{II} + \frac{\nu}{1-2\nu}\mathbf{I}\otimes\mathbf{I}\right) \tag{4}$$

being the tensor of isotropic elastic moduli. E and ν are the Young's modulus and Poisson's ratio, respectively. $\mathbf{E}$ is the Lagrangian strain given by

$$\mathbf{E} = \tfrac{1}{2}(\mathbf{F}^T\cdot\mathbf{F} - \mathbf{I}). \tag{5}$$

Also in the above formulas, $\mathbf{II}$ is the fourth order identity tensor, $\mathbf{I}$ is the second order identity tensor, $\mathbf{I}\otimes\mathbf{I}$ denotes the tensor product of two second order tensors, and $()^T$ and $()^{-T}$ denote inverse and inverse transpose, respectively. The resulting stress-strain relation specifies a linear relation between $\mathbf{S}$ and $\mathbf{E}$, i.e.,

$$\mathbf{S} = \frac{E}{1+\nu}\mathbf{E} + \frac{E\nu}{(1+\nu)(1-2\nu)}(\operatorname{tr}\mathbf{E})\mathbf{I}. \tag{6}$$

Under the conditions of infinitesimal strains, this relation approximates the isotropic, linear elastic behavior. A discussion of linear stress-strain relations for finite deformations is given by Batra (1999).

The constitutive law for cohesive surfaces relates the traction and displacement jumps across crack surfaces and is also taken to be hyperelastic so that any dissipation associated with separation is neglected. Assuming the surface potential energy is ϕ, the traction on the cohesive surfaces can be derived through

$$\mathbf{T} = -\frac{\partial \phi}{\partial \Delta}. \tag{7}$$

In two dimensions, the specific form of ϕ is given by Xu and Needleman (1994) as

$$\phi(\mathbf{\Delta}) = \phi_0 - \phi_0 \left(1 + \frac{\Delta_n}{\delta_n}\right) \exp\left(-\frac{\Delta_n}{\delta_n}\right) \exp\left(-\frac{\Delta_t^2}{\delta_t^2}\right), \tag{8}$$

where $\Delta_n = n \cdot \mathbf{\Delta}$ and $\Delta_t = t \cdot \mathbf{\Delta}$ are the normal and tangential displacement jumps, with $\mathbf{n}$ and $\mathbf{t}$ denoting unit vectors along the surface normal and tangent in the reference configuration, respectively. Potential ϕ is written such that $\phi(\mathbf{\Delta})|_{|\mathbf{\Delta}|=0} = 0$ and therefore $\phi_0 = \phi(\mathbf{\Delta})|_{|\mathbf{\Delta}|\to\infty}$ is the work of separation. Two special paths of decohesion are considered to illustrate the variations of the cohesive traction components. The first path is pure normal separation with tangential traction component $T_t = \mathbf{t} \cdot \mathbf{T} = 0$ and tangential separation $\Delta_t = 0$. The second path is pure tangential separation with normal traction component $T_n = \mathbf{t} \cdot \mathbf{T} = 0$ and normal separation $\Delta_n = 0$. The works of normal and tangential separations along these two paths are equal to each other and are taken to be $\phi_0 = e\sigma_{\max}\delta_n = \sqrt{\frac{e}{2}}\tau_{\max}\delta_t$, with $e = \exp(1) = 2.718281829$. δ_n and $\delta_t/\sqrt{2}$ are normal and shear displacement jump values at which maximum normal stress $\sigma_{\max}$ and maximum shear stress $\tau_{\max}$ occur, respectively.

The cohesive surface traction components obtained from (7) and (8) are

$$T_n(\mathbf{\Delta}) = -\frac{\phi_0 \Delta_n}{\delta_n^2} \exp\left(-\frac{\Delta_n}{\delta_n}\right) \exp\left(-\frac{\Delta_t^2}{\delta_t^2}\right), \tag{9}$$

and

$$T_t(\mathbf{\Delta}) = -\frac{2\phi_0 \Delta_t}{\delta_t^2} \left(1 + \frac{\Delta_n}{\delta_n}\right) \exp\left(-\frac{\Delta_n}{\delta_n}\right) \exp\left(-\frac{\Delta_t^2}{\delta_t^2}\right). \tag{10}$$

These relations are illustrated in Figure 1. Clearly, there are cross dependencies of normal traction (T_n) on shear displacement jump (Δ_t) and shear traction (T_t) on normal displacement jump (Δ_n). In general, the traction components first increase with the displacement jumps and decrease with further increase in separations after displacement jumps exceed certain values. Both traction components approach zero as $|\mathbf{\Delta}| \to \infty$. Figure 1(a) shows the dependence of normal traction T_n on normal separation Δ_n and shear separation Δ_t. When normal separation is attempted while Δ_t is held to be zero ($\Delta_n > 0$ and $\Delta_t = 0$), T_n first increases with Δ_n for $0 < \Delta_n < \delta_n$; it reaches maximum stress $\sigma_{\max}$ at $\Delta_n = \delta_n$, decreases with Δ_n thereafter and approaches zero as Δ_n goes to ∞. A nonzero shear separation Δ_t always reduces the value of T_n required for causing the same amount of normal separation Δ_n. The normal traction component increases rapidly with negative normal separations ($\Delta_n < 0$, representing

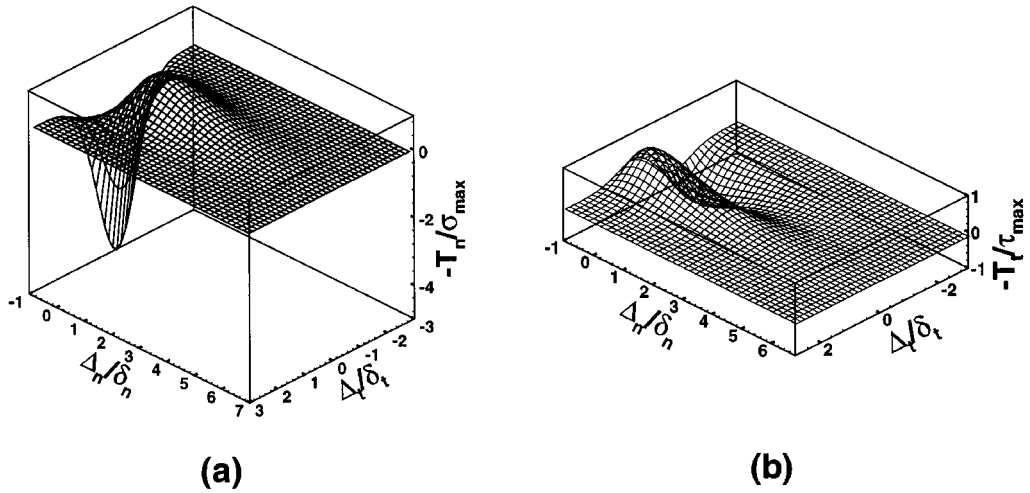

Figure 1. An illustration of the constitutive behavior of cohesive surfaces, (a) normal traction, (b) shear traction.

interpenetration of the crack surfaces). This part of the relation simulates the strong atomistic repulsion during compression. Figure 1(b) shows the variation of T_t with Δ_t and Δ_n. When shear separation is attempted while Δ_n is held to be zero ($\Delta_t \neq 0$ and $\Delta_n = 0$), T_t first increases with $|\Delta_t|$ for $0 < |\Delta_t| < \delta_t/\sqrt{2}$; it reaches maximum stress $\tau_{\max}$ at $|\Delta_t| = \delta_t/\sqrt{2}$, decreases with $|\Delta_t|$ thereafter and approaches zero as $|\Delta_t|$ goes to ∞. A nonzero normal separation Δ_n always reduces the value of T_t required for causing the same amount of shear separation Δ_t.

The balance of energy requires that the total external work $\mathcal{P}$ done to a body to be equal to the sum of the strain energy $\mathcal{W}$ stored in the bulk material, the kinetic energy $\mathcal{K}$ in the body and the cohesive surface energy Φ in crack surfaces, i.e.

$$\mathcal{P} = \int_0^t \int_{S_{\text{ext}}} \mathbf{T} \cdot \frac{\partial \mathbf{u}}{\partial t} \, \mathrm{d}S \, \mathrm{d}t = \mathcal{K} + \mathcal{W} + \Phi, \tag{11}$$

where

$$\left.\begin{aligned} \mathcal{K} &= \textstyle\int_V \frac{1}{2}\rho \dfrac{\partial \mathbf{u}}{\partial t} \cdot \dfrac{\partial \mathbf{u}}{\partial t} \, \mathrm{d}V, \\ \mathcal{W} &= \textstyle\int_V W \, \mathrm{d}V, \\ \Phi &= \textstyle\int_{S_{\text{int}}} \phi \, \mathrm{d}S, \end{aligned}\right\}. \tag{12}$$

Cohesive energy Φ is the amount of energy spent on generating new crack surfaces, therefore represents a measure of the energy consumption on fracture. Under the same loading conditions, the higher the Φ required for generating the same amount of crack surfaces, the higher the fracture resistance of the material. In the analyses carried out there, this energy is used to compare the fracture resistance of specimens with different microstructures under the same overall remote loading.

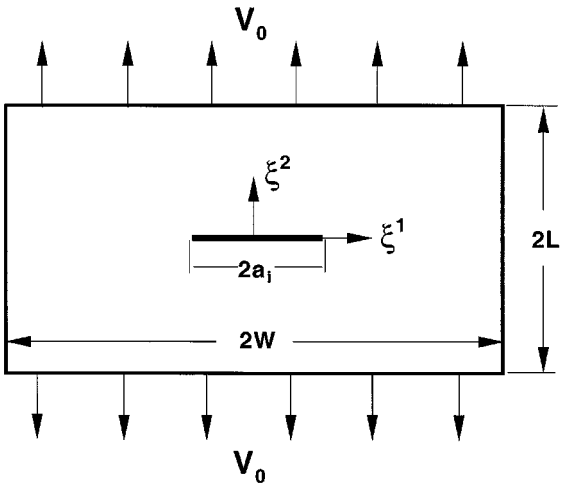

Figure 2. Problem analyzed: a centered-cracked specimen under tensile loading.

3. Problem analyzed

Computations are carried out for a center-cracked specimen, as illustrated in Figure 2. The specimen has an initial height of $2H = 1.6\,\text{mm}$ and an initial width of $2L = 1.6\,\text{mm}$. An initial crack of length $2a_i = 0.4\,\text{mm}$ exists along the ξ^1 axis. Only one half of the specimen ($\xi^1 > 0$) is discretized and modeled in the simulations because of the symmetry with respect to the ξ^2 axis. Conditions of plain strain are assumed to prevail. The small region in front of the crack tip contains microstructures digitized from micrographs of actual composite materials, see Figure 3. Inside this region, the material inhomogeneities and material distribution are explicitly modeled. Digitized microstructures of actual Al_2O_3/TiB_2 composites are used in the analyses. The particular microstructural morphologies analyzed are shown in Figure 4. The microstructure in Figure 4(a) has a TiB_2 grain volume fraction of approximately 32 percent. The average grain size is $10\,\mu$m. This microstructure is referred to as the base microstructure throughout this paper. In addition to the base microstructure, two variations are also considered. The first variation, shown in Figure 4(b), is obtained from the base microstructure by reducing the volume fraction of the TiB_2 grains from 32 to 15 percent. This reduction is achieved by successively removing layers of TiB_2 from the grains and converting them into the matrix material, Al_2O_3. The second variation is shown in Figure 4(c) and is obtained from the base microstructure by shrinking uniformly the constituents in the microstructure. The ratio of reduction is 50 percent in each direction therefore the average grain size in Figure 4(c) is one half of that in Figure 4(a). The volume fractions of the phases, nevertheless, remain the same as those in the base microstructure. Each of the phases behaves hyperelastically according to (2) and (3). Depending on material properties, boundary conditions and loading, fracture is possible inside each of the phases and along the interfaces between the phases. The bulk properties of each finite element are those for either the grains or those for the matrix. The properties of each segment of potential fracture surface are specified according to its location as those belonging to the Al_2O_3 matrix, the TiB_2 grains or the matrix/grain interfaces.

Materials outside the crack-tip region are assumed to be homogeneous and are assigned a set of effective parameters representative of those for the Al_2O_3/TiB_2 ceramic composite. Both regions are discretized in the same manner, using both the bulk and the cohesive surface

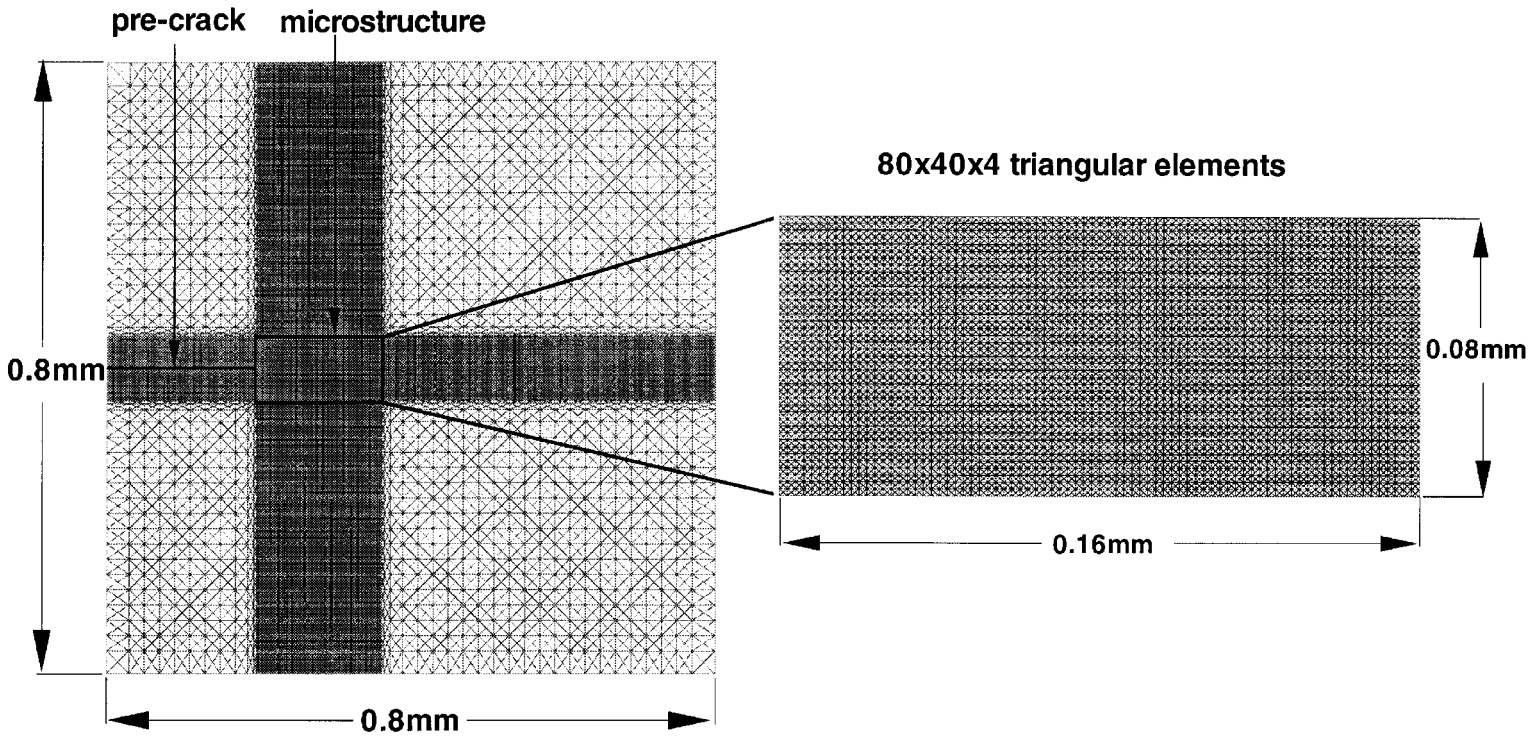

Figure 3. Finite element model and mesh for the specimen.

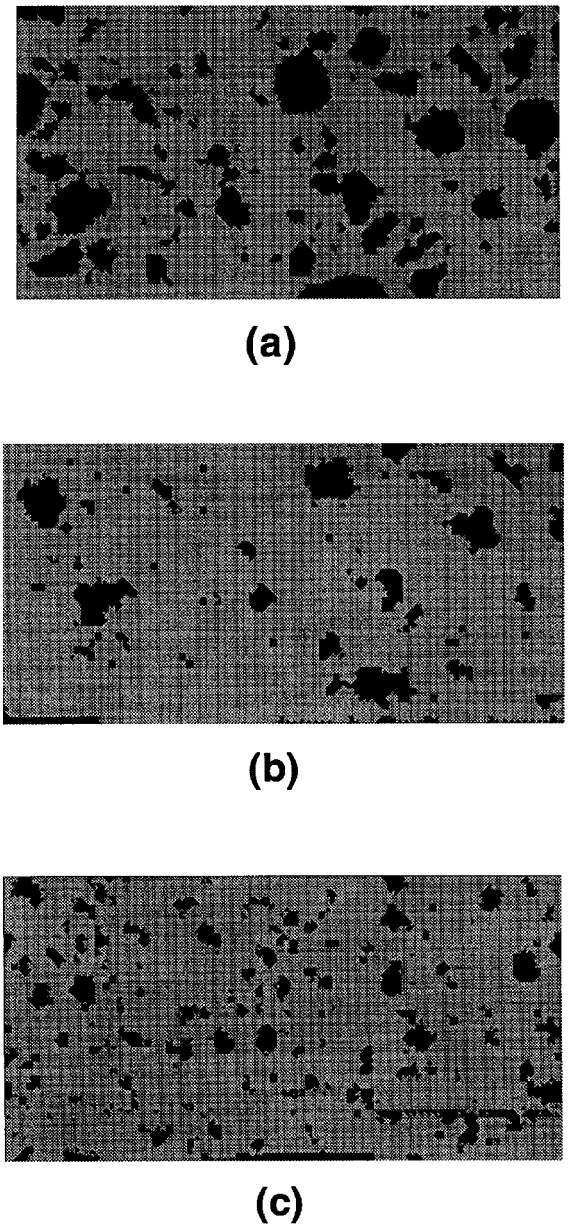

Figure 4. Microstructural morphologies analyzed: (a) base microstructure, (b) lower volume fraction, (c) smaller grain size.

constitutive descriptions. The specimen is stress-free and at rest initially. Tensile loading is applied by imposing symmetric velocity boundary conditions along the upper and lower edges of the specimen. For the results discussed here, the imposed boundary velocity is $V_0 = 50$ m/s for each edge with a linear ramp from zero to this maximum velocity in the first 0.01 μs of

Table 1. Bulk material properties

Compound	Density (Kg/m^3)	K_{IC} (MPa$\sqrt{m}$)	E (GPa)	ν	C_L (m/s)	C_S (m/s)	C_R (m/s)
Al_2O_3	3990	4.0	340	0.23	9939	5885	5379
TiB_2	4520	7.2	500	0.12	10694	7027	6267
Composite	4120	3.6	415	0.15	10300	6609	5936

Table 2. Constitutive parameters for cohesive surfaces

Cohesive surface pair	$\sigma_{\max}$ (GPa)	$\tau_{\max}$ (GPa)	δ_n, δ_t (μ m)	ϕ_0 (J/m^2)
Al_2O_3	34	78.2	0.0005	46.2
TiB_2	50	11.5	0.001	135.9
Composite	41.5	95.5	0.0003	33.8
Al_2O_3 /TiB_2 (Strong Interface)	34	78.2	0.001	92.4
Al_2O_3 /TiB_2 (Weak Interface)	1.7	3.91	0.001	4.6

loading. All other specimen surfaces have traction-free boundary conditions. Specifically, the loading conditions are

$$\dot{u}^2(\xi^1, \pm H, t) = \begin{cases} \pm\dfrac{t}{0.01} V_0, & t < 0.01\,\mu\text{s}, \\ \pm V_0, & t > 0.01\,\mu\text{s}, \end{cases} \quad -L < \xi^1 < L; \tag{13}$$

$$T^1(\xi^1, \pm H, t) = 0, \quad -L < \xi^1 < L; \tag{14}$$

$$T^1(\pm L, \xi^2, t) = T^2(\pm L, \xi^2, t) = 0, \quad -H < \xi^2 < H. \tag{15}$$

The material and model parameters are listed in Table 1 (bulk properties) and Table 2 (cohesive surface constitutive properties). For comparison and analysis purposes, the speeds for the longitudinal stress waves (c_L), the shear stress waves (c_s) and the Rayleigh surface waves (c_R) are also listed in Table 1. The choice of the cohesive law parameters assumes that $\sigma_{\max} = E/10$, with E being the Young's modulus, and $\phi_0 = \frac{(1-\nu^2)K_{IC}^2}{E}$, with K_{IC} being the mode-I fracture toughness of the materials in question.

4. Finite element method

Finite element discretization is based on linear-displacement triangular elements arranged in a 'crossed-triangle' quadrilateral pattern. Neighboring elements are connected through cohesive

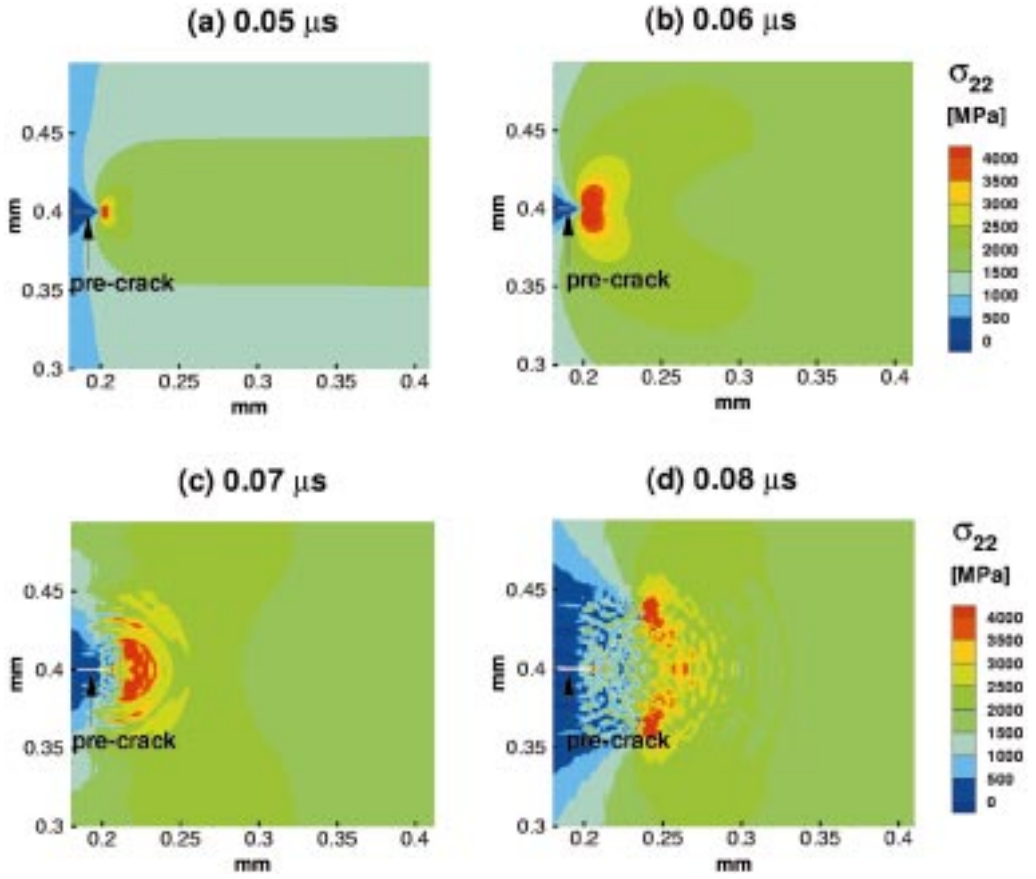

Figure 5. Distributions of σ_{22} at four different times for a specimen of pure Al_2O_3, $V_0 = 50$ m/s.

surfaces. Hence, for the uniform mesh region in front of the crack tip in Figure 3, the cohesive surfaces are initially oriented along four directions, horizontal (0°), vertical (90°), positive and negative 45 degrees (±45°). Since a very fine mesh is used (the element size is 2 μm), arbitrary fracture paths or patterns can be resolved. When the finite element discretization of the displacement field is substituted into the principle of virtual work (1), the discretized equations of motion take the form

$$\mathbf{M}\frac{\partial^2 \mathbf{U}}{\partial t^2} = \mathbf{R}, \tag{16}$$

where **U** is the vector of nodal displacements, **M** is the nodal mass matrix and **R** is the nodal force vector consisting of contributions from the bulk elements and the cohesive surfaces. A lumped mass matrix is used in (16) instead of the consistent mass matrix for reasons of efficiency and accuracy during explicit time-integration, Krieg and Key (1973). The explicit time-integration scheme based on the Newmark β-method with $\beta = 0$ and $\gamma = 0.5$ (Belytschko et al., 1976) is employed to integrate (16).

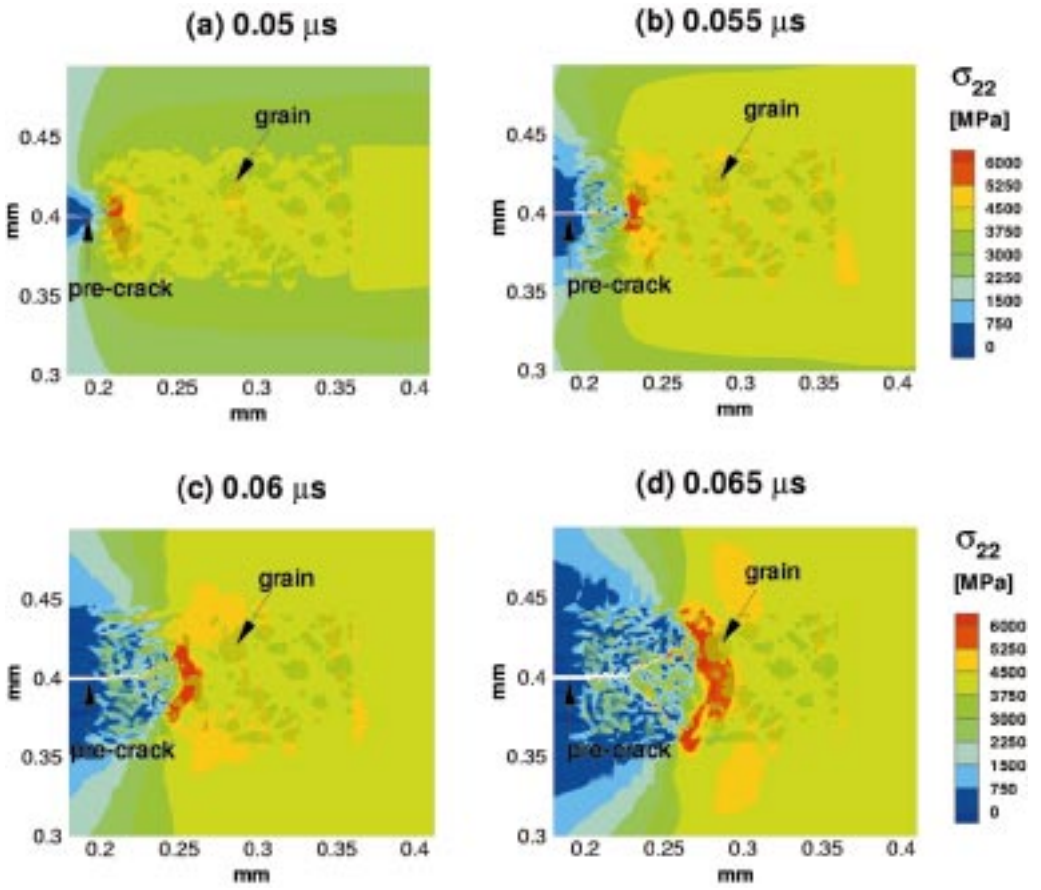

Figure 6. Distributions of σ_{22} at four different times for a specimen with microstructure in Figure 4(a) and a strong interfacial bonding between the grains and the matrix, $V_0 = 50$ m/s.

5. Results

For comparison purposes, a calculation is first carried out for a specimen made of pure Al_2O_3 matrix without reinforcement. The material for the whole specimen has the bulk and cohesive surface properties for Al_2O_3 listed in Tables 1 and 2. This calculation has an applied boundary velocity of $V_0 = 50$ m/s. The distributions of the vertical component of the Cauchy stress σ_{22} at four different times are shown in Figure 5. The location of the tip of the initial crack is at 0.2 mm in the horizontal direction. Crack propagation initiates at approximately 0.065 μs after the beginning of loading. The crack first propagates horizontally briefly and then divides into two propagating branches which are oriented at approximately $\pm 45^\circ$ from the initial direction of propagation. This behavior has been described by Xu and Needleman (1994). The average crack speed in this case is 3200 m/s for the period shown. Note that the Rayleigh wave speed in this material is 5379 m/s.

The results of two calculations using the base microstructure in Figure 4(a) are shown in Figures 6 and 7. These two sets of results are obtained for the same loading condition of $V_0 = 50$ m/s, the same that as in Figure 5. In Figure 6, the interfaces between the grains and the matrix are assumed to have a strong bonding, as characterized by a maximum normal stress of $\sigma_{\max} = 34$ GPa and a maximum shear stress of $\tau_{\max} = 78.2$ GPa. These values correspond to a

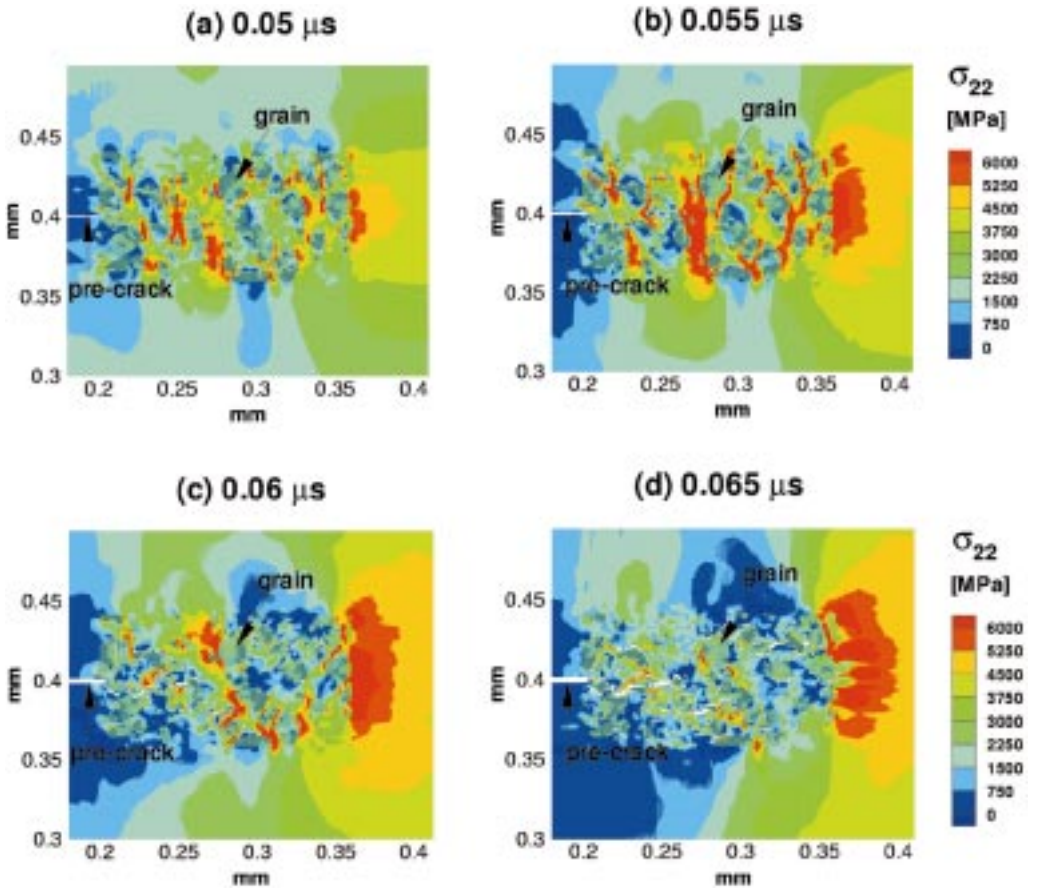

Figure 7. Distributions of σ_{22} at four different times for a specimen with microstructure in Figure 4(a) and a weak interfacial bonding between the grains and the matrix, $V_0 = 50$ m/s.

work of separation of $\phi_0 = 92.4\,\text{J/m}^2$. In Figure 7, the interfaces between the two constituent phases are assumed to have a weak bonding with $\sigma_{\max} = 1.7\,\text{GPa}$, $\tau_{\max} = 3.91\,\text{GPa}$ and $\phi_0 = 4.6\,\text{J/m}^2$.

Figure 6 shows that when strong interfacial strength is assumed fracture occurs through the extension of the pre-existing crack. The crack propagation exhibits a zigzag pattern because of the material inhomogeneities. The crack eventually splits into two branches, in a way similar to what is seen in Figure 5 for fracture in uniform Al_2O_3. However, the crack extension before branching is longer than that in Figure 5. The crack propagation occurs mainly in the matrix and along grain-matrix interfaces, with occasional fracture of grains. In Figure 7, the mode of failure is initiation, growth and coalescence of microcracks. Clearly, the relatively weak interfacial bonding allows microcracks to initiate at multiple interfacial sites upon tensile loading. This process can occur independently of the main pre-crack. Coalesced microcracks eventually link up with the main crack, resulting in the failure of the material.

The evolutions of the crack lengths for the three cases discussed so far are compared in Figure 8. The curves represent the histories of the cumulative length of cracks/microcracks in each constituent or along the phase boundaries, regardless of the number of segments involved. The history of combined total crack length in all fracture sites is also shown. The cumulative

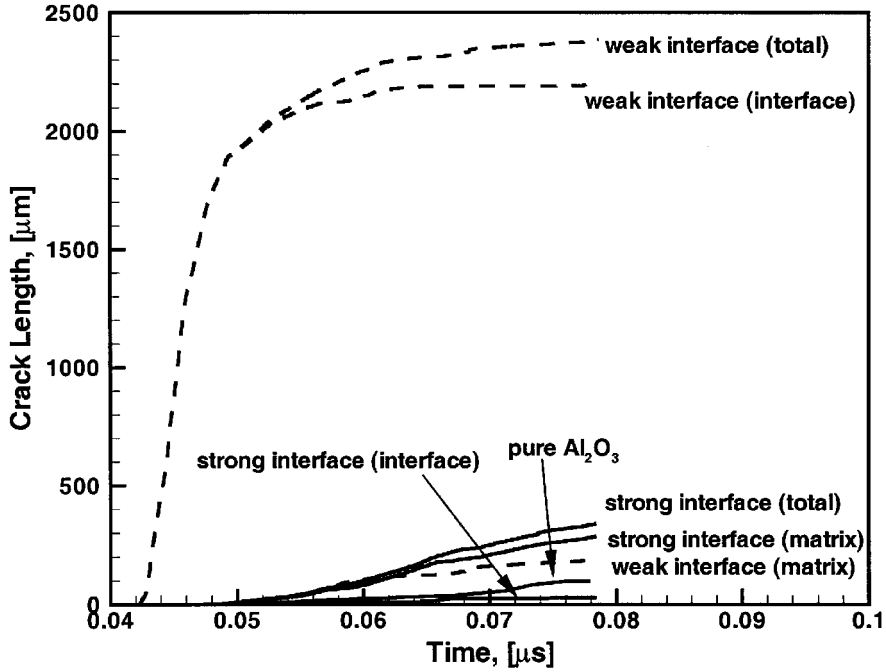

Figure 8. A comparison of crack length histories for the cases in Figures 5–7.

crack length in the grains is quite small and is, therefore, not plotted. The specimen made of pure Al_2O_3 shows the smallest crack length at all stages of deformation. Clearly, material inhomogeneities allowed significantly more crack surfaces to be generated under the same remote deformation. The total amount of crack surface area generated in Figure 6 with the strong interfacial bonding is approximately three times ($\sim 300\,\mu$m at $0.08\,\mu$s) that in Figure 5 ($\sim 100\,\mu$m at $0.08\,\mu$s). The total crack surface area for the weak interface in Figure 7 is 24 times ($\sim 2400\,\mu$m at $0.08\,\mu$s) that in Figure 5. There is a difference in the distributions of fracture sites in the two cases as well. In Figure 6, the strong interfaces cause cracks to propagate predominantly in the matrix. While in Figure 7, the weak interphase bonding allows microcracks to form mainly through grain-matrix interfacial debonding. The results here are consistent with experimental observations that materials with strong interphase bonding show transgranular fracture and materials with weak interphase bonding show intergranular fracture, Logan (1996).

The work of separation for the weak interface is only 1/20 that for the strong interface (see Table 2), corresponding to significantly less energy consumption per unit crack surface area generated. However, the higher amount of crack surface seen in Figure 8 more than compensates for this lower energy value per unit area. Figure 9 shows the evolutions of the strain energy stored in the specimen materials, the kinetic energy in the specimen and the cohesive energy or surface energy along cracks generated. It can be seen that the rate of energy dissipation through crack surface generation is actually higher initially for weak interfaces. This is due to the simultaneous occurrence of microcracks in multiple locations. Consequently, more energy is delivered into the crack surfaces during this time period than in the case of strong interfaces. As crack growth continues, the cohesive energy (Φ) for the strong interface material eventually exceeds that for the weak interface case. The mode of failure through microcracks also corresponds to less strain energy ($\mathcal{W}$) in the specimen and a higher

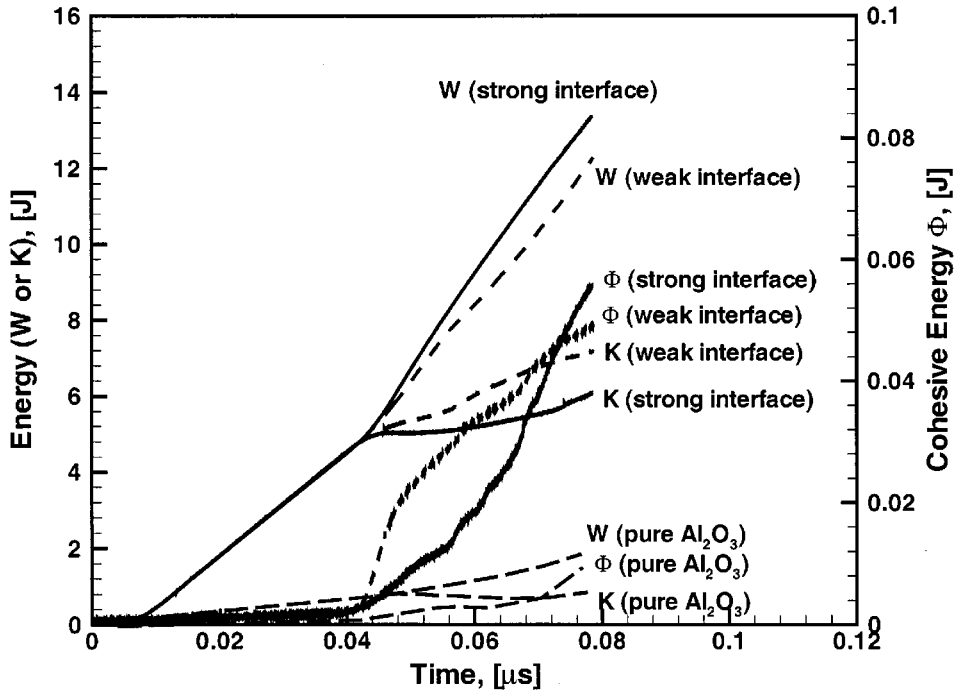

Figure 9. A comparison of energy evolutions for the cases in Figures 5–7.

amount of kinetic energy ($\mathcal{K}$) in the bulk material. The effect of TiB_2 reinforcements on the energies is clearly significant regardless of the interfacial strength. Without the reinforcements or grains, all energies are only small fractions of the values for the cases with reinforcements. For example, the cohesive surface energy (Φ) for the pure matrix material is only $\frac{1}{5}$ of those for the composites, see Figure 9.

The distributions of σ_{22} at four different times for two calculations using the microstructures in Figure 4(b, c) are shown in Figures 10 and 11, respectively. Here, the same strong interphase bonding strength as that in Figure 6 is assumed. It can be seen that reducing the grain volume fraction and reducing the grain size while keeping the grain volume fraction constant have similar effects of facilitating the propagation of the pre-crack and expediting its subsequent branching into multiple cracks. The smaller number of grains and the smaller size of grains pose less impediment to the propagation of cracks. Indeed, the results in these figures look closer to the results in Figure 5 than to the results in Figure 7.

The crack length histories for Figures 6, 10 and 11 are shown in Figure 12. These curves allow the effects of the different microstructures in Figure 4 to be compared quantitatively. Consistent with what is seen in Figures 10 and 11, the lower grain volume fraction for microstructure *B* and smaller grain size for microstructure *C* both cause the crack length in the matrix to increase. The result is higher overall crack lengths for microstructures *B* and *C*. These variations in microstructure do not seem to show a clear influence on the amount of interfacial crack or microcrack growth under the conditions analyzed. The corresponding energy evolutions for the three cases are shown in Figure 13. As a result of the increases in the matrix crack lengths, microstructures *B* and *C* have slightly higher cohesive energy levels than microstructure *A*. These results suggest that the variation of cohesive energy with grain

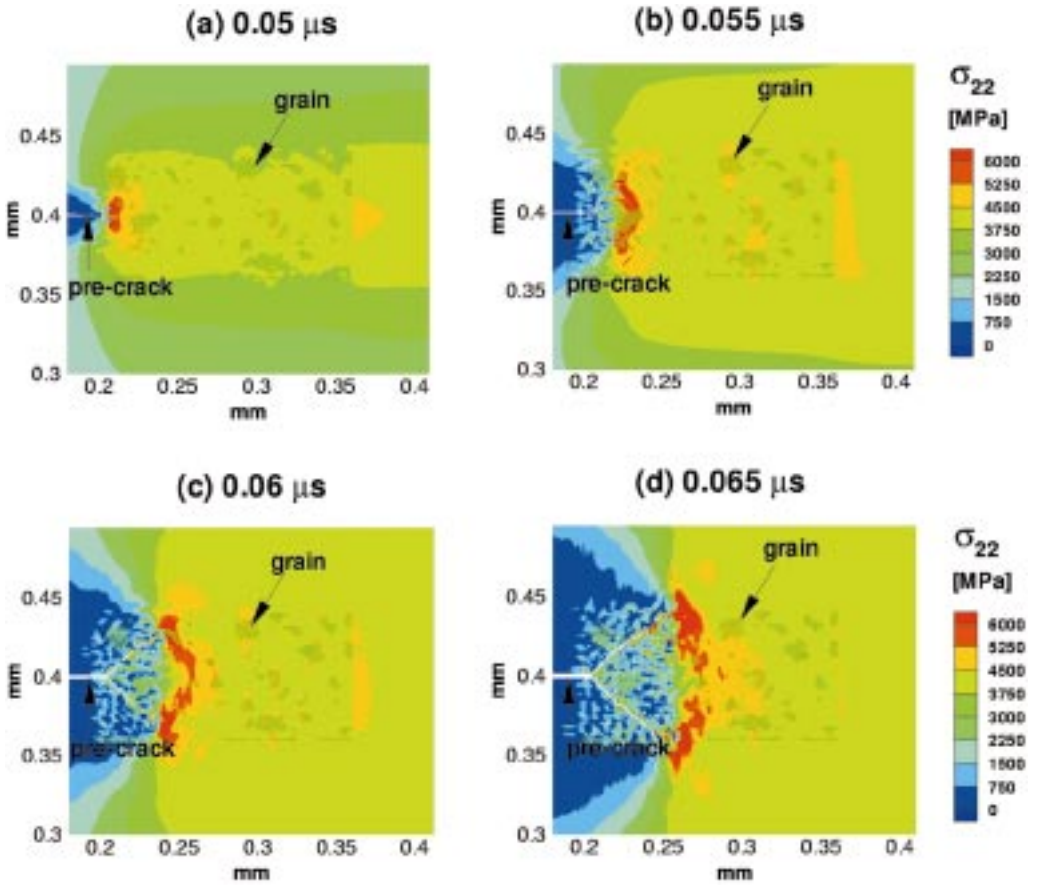

Figure 10. Distributions of σ_{22} at four different times for a specimen with microstructure in Figure 4(b) and a strong interfacial bonding between the grains and the matrix, $V_0 = 50$ m/s.

size or grain volume fraction may not be monotonic. Rather, phase distributions and phase morphologies may have an impact. This effect has been analyzed in Zhai and Zhou (1998).

6. Discussion and conclusions

A micromechanical framework of analysis has been developed and used to provide explicit incorporation of arbitrary material microstructures and to resolve arbitrary, unconstrained fracture patterns in heterogeneous, brittle solids. The approach combines descriptions of bulk constituent response and fracture surface cohesion, as originally used by Xu and Needleman (1994). This approach is especially appropriate for analyzing microscopic failure and fracture over a range of length scales because material separation is a natural outcome of constitutive behavior, microstructure and loading in this model. The formulation is free from failure criteria valid over only certain length scales, e.g., continuum criteria based on the existence of K-fields.

The dynamic failure behavior in a class of Al_2O_3/TiB_2 composites is simulated under the context of a centered-cracked specimen and the conditions of plane strain. In this analysis, both the bulk and interfacial constitutive laws are hyperelastic. The results demonstrated the effects of microstructure on dynamic failure in the materials. The bonding strength between

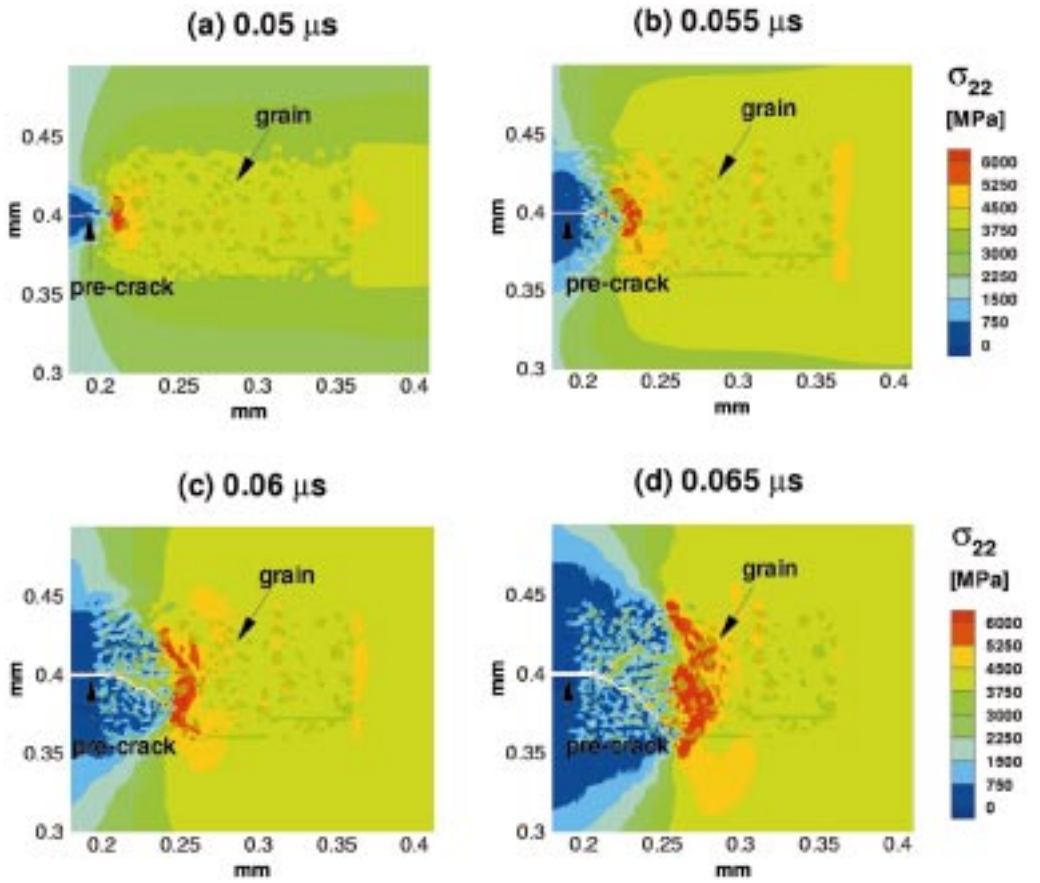

Figure 11. Distributions of σ_{22} at four different times for a specimen with microstructure in Figure 4(c) and a strong interfacial bonding between the grains and the matrix, $V_0 = 50$ m/s.

the alumina matrix and the titanium diboride reinforcements, which is a function of conditions during hot-pressing of the composites, is found to significantly influence the failure modes in the composites. When strong bonding exists, the mode of failure is the extension of cracks and crack branching. When weak bonding exists, the mode of failure is microcrack growth and coalescence. The framework of analysis also allows the evolution of crack lengths and the evolution of energies to be tracked. Calculations have shown that under the same overall remote deformation microscopic TiB_2 reinforcements significantly increase the total cohesive energy consumed in the generation of crack and microcrack surfaces.

Acknowledgement

Support from the U.S. Army Research Office through grant DAAG55-98-1-0454 is gratefully acknowledged. Calculations reported are carried out on the Cray Computers at the San Diego Supercomputer Center, Jet Propulsion Laboratory and the Goddard Space Center. M.Z. would like to thank Prof. A. Needleman and Dr. X.-P. Xu for helpful discussions. Thanks are extended to Dr. K.V. Logan for providing micrographs of Al_2O_3/TiB_2 composites used in this research.

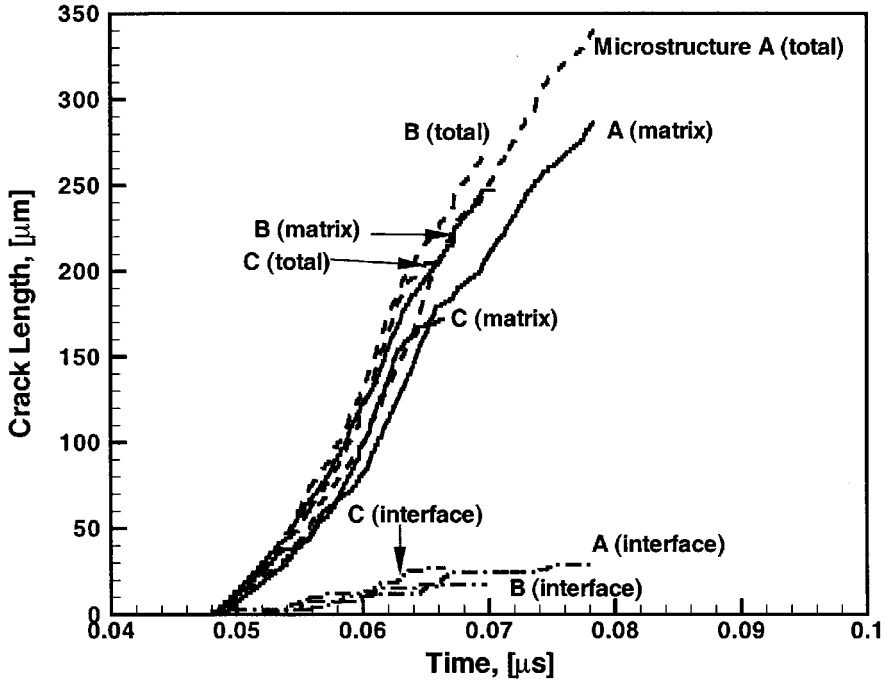

Figure 12. A comparison of crack length histories for the three different microstructures in Figure 4.

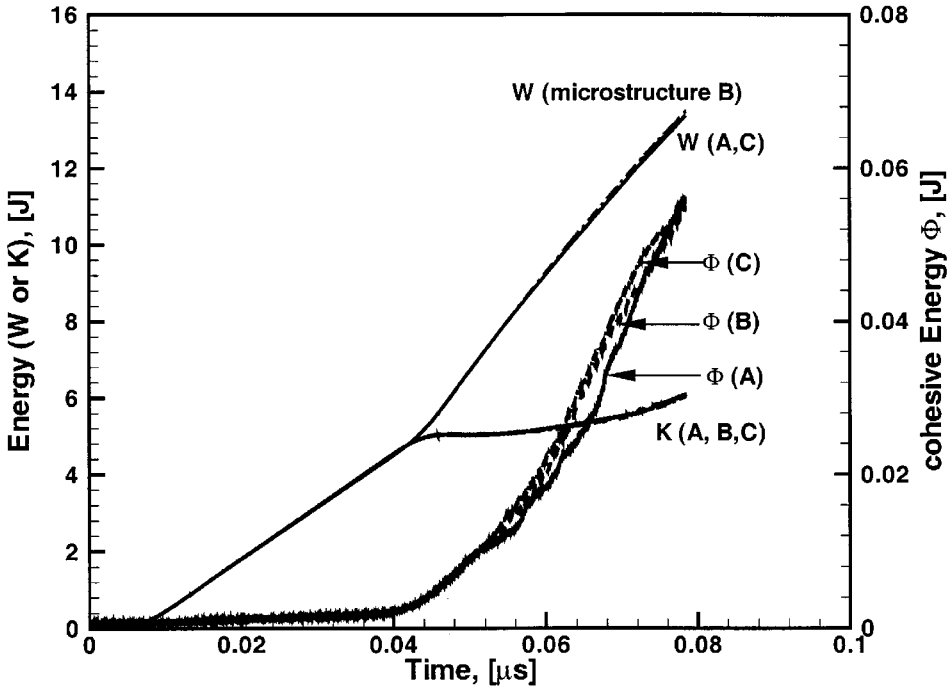

Figure 13. A comparison of energy evolutions for the three different microstructures in Figure 4.

References

Ahrens, T.J. and Rubin, A.M. (1983). Impact-induced tensional failure in rock. *Journal of Geophysics Research* **98**, 1185–1203.

Barrenblatt, G.I. (1962). The mathematical theory of equilibrium of cracks in brittle fracture. *Advanced Applied Mechanics* **7**, 55–192.

Batra, R.C. (1998). Linear constitutive relations in isotropic finite elasticity. *Journal of Elasticity* **52**(1), 75–90.

Belytschko, T., Chiapetta, R.L. and Bartel, H.D. (1976). Efficient large scale non-linear transient analysis by finite elements. *International Journal of Numerical Methods in Engineering* **10**, 579–596.

Brockenbrough, J.R., Suresh, S. and Duffy, J. (1988). An analysis of dynamic fracture in microcracking solids. *Philosophical Magazine A* **58**, 619–634.

Camcho, G.T and Ortiz, M. (1996). Computational modeling of impact damage in brittle materials. *International Journal of Solids and Structures* **33**(20-22), 2899–2983.

Curran, D.R., Seaman, L., Cooper, T. and Shockey, D.A. (1993). Micromechanical model for continuum and granular flow of brittle materials under high strain rate application to penetration of ceramic targets. *International Journal of Impact Engineering* **13**, 53–58.

Curran, D.R., Seaman, L. and Shockey, D.A. (1987). Dynamic failure of solids. *Physics, Reports* **147**, 253–388.

Curtin, W. (1991). Theory of mechanical properties of ceramic-matrix composites. *Journal of the American Ceramic Society* **74**, 2837–2845.

Dugdale, D.S. (1960). Yielding of steel sheets containing slits. *Journal of Mechanics and Physics of Solids* **8**, 100–104.

Espinosa, H.D., Raiser, G., Clifton, R.J. and Ortiz, M. (1992). Experimental observation and numerical modeling of inelasticity in dynamic loaded ceramics. *Journal of Hard Materials* **3**, 285–313.

Espinosa, H.D. and Brar, N.S. (1995). Dynamic failure mechanisms of ceramic bars: Experiments and numerical simulations. *Journal of Mechanics and Physics of Solids* **43**, 1615–1638.

Evans, A.G. (1991). The mechanical properties of reinforced ceramic, metal and intermetallic matrix composites. *Materials Science and Engineering A* **143**, 63–76.

Gao, H.J. and Klein, P. (1997). Numerical simulation of crack growth in an isotropic solid with randomized cohesive bonds. *Journal of Mechanics and Physics of Solids* (to appear).

Grady, D.E. and Kipp, M.E. (1979). The micromechanics of impact fracture of rock. *International Journal of Rock Mechanics* **16**, 293–302.

Johnson, G.R. and Holmquist, T.J. (1992). A computational constitutive model for brittle materials subjected to large strains, high rates, and high pressure. *Shock Wave and High Strain Rate Phenomena in Materials* (Edited by Meyers, M.A., Murr, L.E. and Staudhammer, K.P.), 1075–1081.

Jones, D.W. (1996). Ceramic biomaterials. *Key Engineering Materials* **122-124**, 345–384.

Kishi, T., Takeda, N. and Kim, B.N. (1990). Dynamic fracture toughness and microstructural fracture mechanisms in ceramics. *Ceramic Engineering of Science Process* **11**(7-8), 650–664.

Kishi, T. (1991). Dynamic fracture toughness in ceramic and ceramics matrix composites. *Engineering Fracture Mechanics* **40**, 785–790.

Kobayashi, A.S. (1991). Dynamic fracture of ceramics and ceramic composites. *Materials Science and Engineering A* **143**, 111–117.

Komanduri, R. (1989). Advanced ceramic tool materials for machining. *International Journal of Refraction Hardening Metals* **8**, 125–132.

Krieg, R.D. and Key, S.W. (1973). Transient shell response by numerical time integration. *International Journal of Numerical Methods in Engineering* **7**, 273–286.

Lange, F.F. (1979). Fracture toughness of Si_3N_4 as function of initial a-phase content. *Journal of the American Ceramic Society* **62**, 428.

Lankford, J. (1989). Dynamic compressive fracture in fiber-reinforced ceramic matrix composites. *Material Science and Engineering A: Structural Materials: Properties, Microstructure and Processing A* **107**, 261–268.

Lankford, J. (1994). Effect of hydrostatic pressure and loading rate on compressive failure of fiber-reinforced ceramic-matrix composites. *Composite Science Technology* **51**, 537–543.

Lehman, R.L. (1989). Ceramic matrix fiber composites. *Treatise Material Science Technology* **29**, 229–191.

Logan, K.V. (1996). *Composite Ceramics, Final Technical Report*. USSTACOM DAAEO7-95-C-R040.

Longy, F. and Cagnoux, J. (1989). Plasticity and microcracking in shock-loaded alumina. *Journal of the American Ceramic Society* **72**, 971–979.

Matsui, M. and Masuda, M. (1994). Fracture behavior of silicon nitride at elevated temperatures. *Tailoring of Mechanical Properties of Si_3N_4 Ceramic* (Edited by M.J. Hoffmann and G. Petzow), Kluwer Academic Publishers, Dordrecht, Netherlands, 403–414.

Messer, P.F. (1991). The strength of dental ceramics. *Journal of Density* **18**, 227–235.

Niihara, K. and Nakahira, A. (1990). Particulate strengthened oxide nanocomposites. *Advanced Structural Inorganic Composites* (Edited by P. Vincenzini), Elsevier publishers, 637–664.

Niihara, K. (1991). New design concepts of structural ceramics-ceramic nanocomposites, the centennial issue of the ceramic society of Japan. *Journal of Ceramic Society of Japan* **99**(10), 974–982.

Niihara, K., Nakahira, A. and Sekino, T. (1993). New nanocomposite structural ceramics. *Material Reserves Society of Symplectic Procedures* **286**, 405–412.

Ortiz, M. (1996). Computational micromechanics. *Computational Mechanics* **18**, 321–338.

Rajendran, A.M. (1994). Modeling the impact behavior of AD85, ceramic under multiaxial loading. *International Journal of Impact Engineering* **15**, 749–768.

Ravichandran, G. and Subhash, G. (1995). A micromechanical model for high strain rate behavior of ceramics. *International Journal of Solids and Structures* **32**, 2627–2646.

Seaman, L., Curran, D.R. and Murri, W.J. (1985). A continuum model for dynamic tensile microstructure and fragmentation. *Journal of Applied Mechanics*, **52**, 593–600.

Shockey, D.A., Curran, D.R., Seaman, L., Rosenberg, J.T. and Peterson, S.F. (1974). Fragmentation of rock under dynamic loads. *International Journal of Rock Mechanics* **11**, 303–317.

Shockey, D.A., Machand, A.H., Skaggs, S.R., Cort, G.E., Burkett, M.W. and Parker, R. (1990). Failure phenomenology of confined ceramic targets and impact rods. *International Journal of Impact Engineering* **9**, 263–275.

Shockey, D.A., Seaman, L. and Curran, D.R. (1985). The micro-statistical fracture mechanics approach to dynamic fracture problems. *International Journal of Fracture* **27**, 145–157.

Suresh, S., Nakamura, T., Yeshurun, Y. Yang, K. H. and Duffy, J. (1990). Tensile fracture toughness of ceramic materials: Effects of dynamic loading and elevated temperatures. *Journal of the American Ceramic Society* **73**, 2457–2466.

Vekinis, G., Ashby, M.F., Shercliff, H. and Beaumont, P.W. (1993). The micromechanisms of fracture of alumina and ceramic-based fiber composite: Modelling the failure processes. *Composites Science and Technology* **48**, 325–330.

Walter, J. (1992). *Material Modeling for Terminal Ballistic Simulation*, Tech. Report, US Army Research Lab., Maryland.

Willmann, G. (1996a). Development in medical-grade alumina during the past two decades. *Journal of Material Processing Technology* **56**, 168–176.

Willmann, G. (1996b). Clinical failure of alumina. *Journal of Arthroplasty* **10**, 855–859.

Woodward, R.L., Gooch, W.A., O'Donnell, R.G., Oerciballi, W.J., Baxter, B.J. and Oattie, S.D. (1994). A study of fragmentation in the ballistic impact of ceramics. *International Journal of Impact Engineering* **15**, 605–618.

Xu, X.-P. and Needleman, A. (1994). Numerical simulations of fast crack growth in brittle solids. *Journal of Mechanics and Physics of Solids* **42**, 1397–1434.

Xu, X.-P., Needleman, A. and Abraham, F.F. (1997). Effect of inhomogeneities on dynamic crack growth in an elastic solid. *Modeling and Simulation Material's Science and Engineering* **5**, 489–516.

Yang, Kwan-Ho, Kobayashi, A.S. (1990). Dynamic fracture response of alumina and two ceramic composites. *Journal of the American Ceramic Society* **73**(8), 2309–2315.

Zeng, J., Tanaka, I., Miyamoto, Y., Yamada, O. and Niihara, K. (1992). Sintering behaviors of Si3N4-silica ceramics during hot isostatic pressing. *Journal of the American Ceramic Society* **75**(1), 148–152.

Zhai, J. and Zhou, M. (1998). Micromechanical modeling of dynamic crack growth in ceramic composites. *Mixed Mode Crack Behavior* (Edited by K. Miller and D.L. McDowell), ASTM STP 1359, 174–202.

Zhao, J., Stearns, L.C., Harmer, M.P., Chan, H.M. and Miller, G.A. (1993). Mechanical behavior of alumina-silicon carbide nanocomposites. *Journal of the American Ceramic Society* **76**(2), 503–510.

Zhou, S.J. and Curtin, W.A. (1995). Failure of fiber composites: A lattice green function model. *Acta Metallurgica et Materialia* **43**, 3093–3104.